

Enabling Ultrasonic Spray Coating of Uniform and Compact 1.6 eV CsFAPbI₃ Films for Efficient Perovskite Solar Cells by Controlling the Wet-to-Dry Film Transition

Joost Caeyers,* Tamara Merckx, Jessica de Wild, Wim Deferme, and Bart Vermang



Cite This: *ACS Appl. Energy Mater.* 2025, 8, 6655–6661



Read Online

ACCESS |

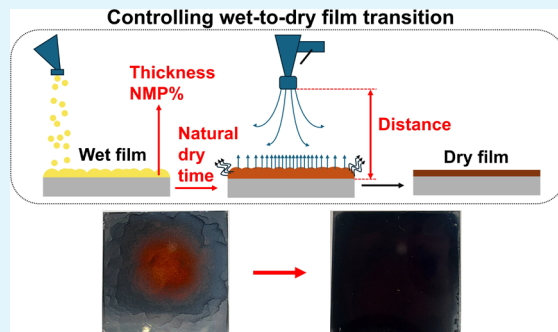
Metrics & More

Article Recommendations

Supporting Information

ABSTRACT: In this study, uniform and compact ultrasonically spray-coated 1.6 eV CsFAPbI₃ films were developed by precisely controlling the wet-to-dry film transition. Achieving both fast nucleation—essential for film compactness—and a smooth wet-to-dry transition to enhance uniformity is particularly challenging in the ultrasonic spray coating of perovskite (PSK). The rapid solvent evaporation via gas quenching, required for achieving fast nucleation, can induce fluid flows that disrupt the film's uniformity, especially in ultrasonic spray coating processes, where the wet film often exhibits thickness variations. Key parameters—including substrate temperature, N₂ gun distance, natural drying time, nozzle path speed, and cosolvent ratio—were adjusted to control the wet-to-dry film transition and suppress unwanted fluid flows. These fluid flows are triggered by the impact of the N₂ flow during gas quenching and are also potentially driven by surface tension gradients. The optimized conditions resulted in a uniform and pinhole-free PSK layer. Integrating the developed PSK film in a completely scalable device stack resulted in uniform performance across the sample's area. The devices showed reproducible power conversion efficiency (PCE) values centered around 17%.

KEYWORDS: perovskite, solar cell, ultrasonic spray coating, wet-to-dry transition, film uniformity, film compactness



INTRODUCTION

Ultrasonic spray coating is an attractive and scalable deposition method for producing PSK films. In ultrasonic spray coating, a spray nozzle moves relative to a substrate while spraying micron-sized droplets. Ultrasonic spray coating achieves high utilization efficiency of the PSK precursor solution, while rapid movement of the spray nozzle enables high-speed film preparation.^{1,2} Additionally, the nondirect contact between the spray nozzle and the substrate makes ultrasonic spray coating an interesting method for both planar and nonplanar rigid substrates, as well as for flexible substrates.

Recent advancements have led to impressive efficiencies in ultrasonically spray-coated perovskite solar cells (PSCs), with a record of 22.43%.³ This study focuses on a 1.6 eV Cs_{0.18}FA_{0.82}Pb(I_{0.94}Br_{0.06})₃ PSK composition, which is particularly suitable for tandem applications when paired with lower band gap semiconductors, such as copper indium gallium selenide (CIGS). Recent research in our group demonstrated promising results, achieving efficiencies close to 20%.⁴

Despite these advances, achieving uniform and compact PSK films with ultrasonic spray coating remains challenging due to uncontrolled drying, which can induce fluid flows that disrupt film uniformity. Gas quenching, a technique that accelerates solvent evaporation, is commonly used to promote fast nucleation and compact film formation. This rapid drying

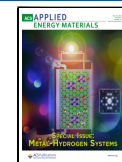
process can cause fluid flows in the wet film either due to the impact of the gas flow or due to Marangoni flows—surface-tension-driven flows caused by variations in solvent evaporation rates across the wet film. In an NMP/DMF cosolvent system, DMF evaporates faster than NMP. Since the surface tension of DMF and NMP is different, this creates a surface tension gradient, causing liquid to flow from DMF-rich areas (lower surface tension) to NMP-rich areas (higher surface tension).⁵ In droplet-based deposition techniques, such as spray coating, the resulting wet film often exhibits greater thickness variations compared to, e.g., blade-coated wet films. These thickness variations may increase the amount of uncontrolled, nonuniform solvent evaporation, thereby further enhancing Marangoni flows. These flows can disrupt the film uniformity during the wet-to-dry film transition, making it challenging to achieve a smooth PSK layer. Controlling both the wet-to-dry film transition and PSK crystallization is a

Received: March 11, 2025

Revised: April 15, 2025

Accepted: April 24, 2025

Published: May 7, 2025



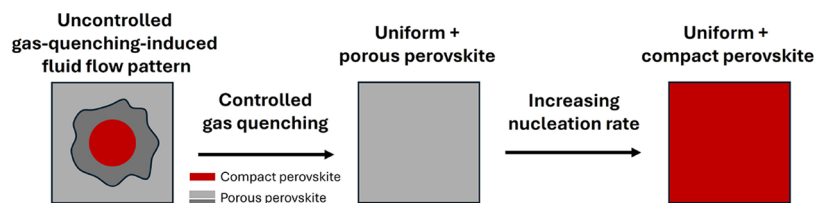


Figure 1. Scheme indicates the approach used to obtain a uniform and compact PSK film.

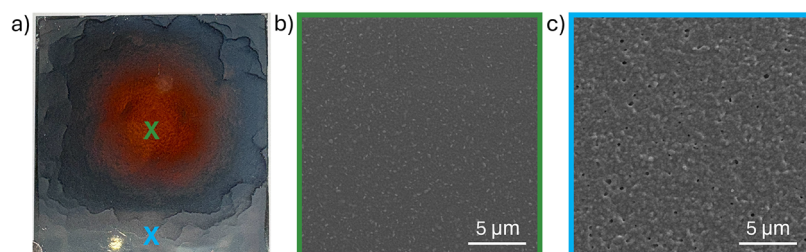


Figure 2. (a) Image of a nonuniform PSK film obtained with the initial set of ultrasonic spray coating parameters on a 3 cm × 3 cm sample. (b,c) SEM images in the dark red circle and at the gray edges, corresponding to the green and blue crosses in panel (a).

central topic in ongoing research on PSK spray coating. Various strategies have been proposed to address these challenges, including tuning the solvent system and tailoring the vapor environment to regulate drying dynamics and promote the formation of uniform, compact PSK films.^{3,6,7}

In this study, we address these challenges by adjusting key process parameters to control the wet-to-dry film transition and suppress disruptive fluid flows. The parameter adjustments were performed guided by visual and morphological inspection, as well as by theoretical concepts such as the LaMer model for nucleation and findings from the literature. Figure 1 illustrates the approach followed. The starting point (the initial recipe) was based on the recipe which delivered the best in-house results coming from previous work in our group.⁸ This recipe, however, resulted in a highly nonuniform PSK film having a compact region in the center and porous areas toward the edges, separated by a visible dried fluid flow pattern, as illustrated on the left in Figure 1. First, process parameters impacting the viscosity of the wet film at the start of the gas quench, as well as the impact of the N₂ flow during the gas quench, were adjusted to suppress fluid flows in the wet film. After fluid dynamics were controlled and film uniformity was achieved, the PSK film remained highly porous due to insufficient quenching, as shown in the middle of Figure 1. The next step involved increasing the nucleation rate to achieve a compact PSK film by further adjusting ultrasonic spray coating parameters. This resulted in a uniform, pinhole-free PSK film over the complete sample area (3 cm × 3 cm), as illustrated on the right in Figure 1. The film was tested in a device stack and showed uniform performance across the sample area. Furthermore, the devices showed reproducible performance across 8 samples, with an average efficiency close to 17%. A champion device achieved a PCE of 18.63%. Our findings establish a reliable method for scalable and high-performance PSC fabrication with ultrasonic spray coating.

RESULTS AND DISCUSSION

Ultrasonic Spray Coating Parameter Adjustments. In the initial phase of this study, relevant ultrasonic spray coating parameters were adjusted to achieve a compact and uniform PSK layer over the entire 3 cm × 3 cm sample surface. The key

parameters are the substrate temperature, N₂ gun distance, natural drying time (i.e., the time interval between the moment the spray nozzle has passed over the entire sample and the start of gas quenching), the nozzle path speed, and NMP concentration, as these parameters significantly influence the wet-to-dry film transition. The initial ultrasonic spray coating recipe included a substrate temperature of 40 °C, a nozzle path speed of 3 cm/s, a N₂ gun distance of 2 cm, a natural drying time of 10 s, and an NMP concentration of 15%. All other ultrasonic spray coating parameters remained constant for all samples made in this study and are listed in the **Experimental Section**. PSK films fabricated during the parameter adjustment process were annealed under identical conditions. Figure 2a shows an image of a PSK film deposited with the parameters, as mentioned above. Clearly, the PSK film is highly nonuniform. Nonuniformity arises during gas quenching due to the impact of the N₂ flow or surface-tension-driven flows, which lead to substantial solute migration from the center to the edges. The film exhibits a dark red circle in the middle of the sample, as indicated by the green cross, underneath the position of the N₂ gun. Figure 2b shows an SEM image of the PSK film in this circle, indicating a compact PSK film. Near the edges, the PSK film is colored grayish, as indicated by the blue cross. Figure 2c shows an SEM image of the PSK film in this region, indicating that the PSK film is highly porous. The results indicate that efficient gas quenching occurs only directly beneath the N₂ gun, producing a compact PSK layer. When moving toward the edges of the film, the N₂ flow is saturated with evaporated solvents, causing inefficient quenching, leading to a porous region. Furthermore, the solute flow toward the outside also increases the wet film thickness, which makes the quenching less efficient (more solvent needs to be evaporated when the wet film is thicker). To mitigate solute flow during gas quenching, the viscosity of the wet film can be increased. This adjustment can be achieved by reducing the substrate temperature to 28 °C.^{9,10} Lowering the temperature also reduces the thermal gradients in the wet film, minimizing nonuniform solvent evaporation and thermally induced surface tension gradients. Additionally, variations in the natural drying time and distance between the N₂ gun and the sample were explored. By increasing the natural drying time, more solvents

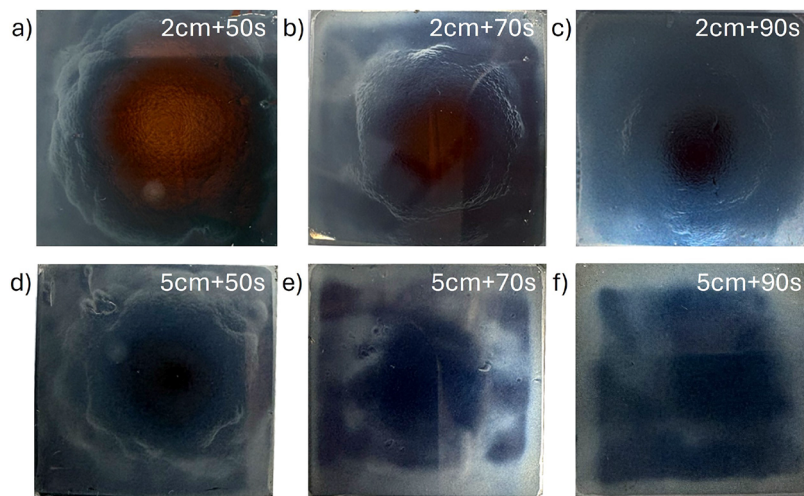


Figure 3. (a–f) Images of PSK films fabricated with N_2 gun distances and natural drying times of (a) 2 cm and 50 s, (b) 2 cm and 70 s, (c) 2 cm and 90 s, (d) 5 cm and 50 s, (e) 5 cm and 70 s, and (f) 5 cm and 90 s, all on a 3 cm \times 3 cm sample.

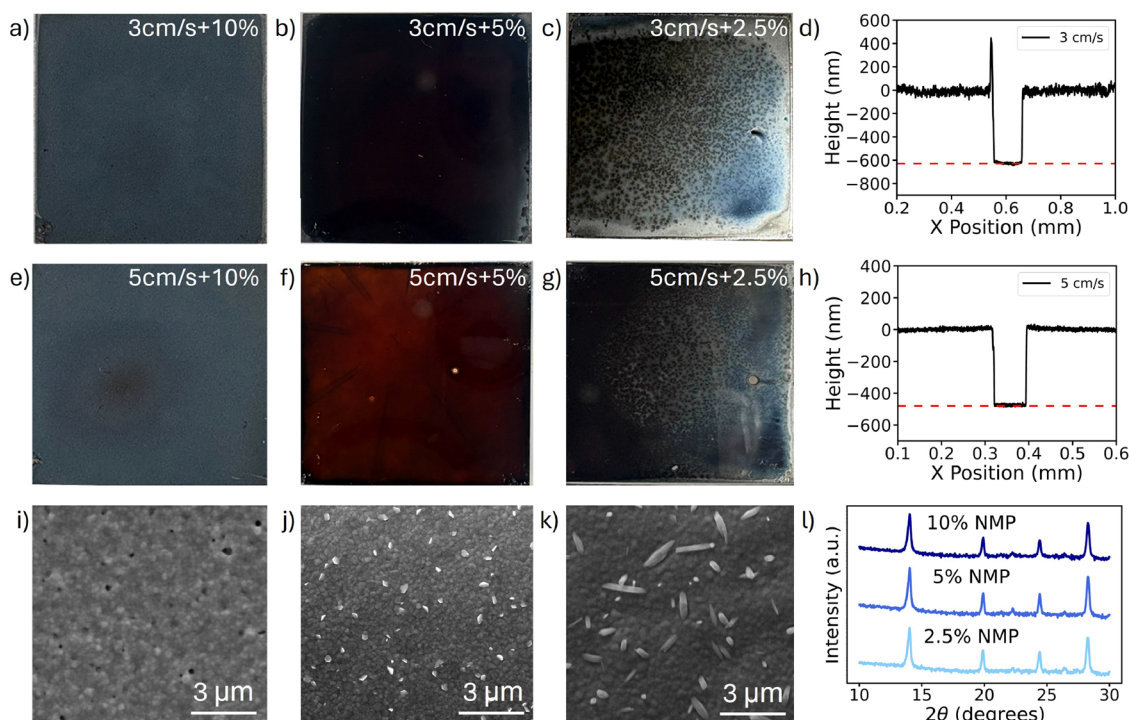


Figure 4. (a–c,e–g) Images of PSK films fabricated with nozzle path speeds and NMP concentrations as follows: (a) 3 cm/s and 10%, (b) 3 cm/s and 5%, (c) 3 cm/s and 2.5%, (e) 5 cm/s and 10%, (f) 5 cm/s and 5%, and (g) 5 cm/s and 2.5%, all on a 3 cm \times 3 cm sample. (d,h) Height measurements on a pure PSK film prepared as in panel (b) and a PSK–ETL film prepared as in panel (f). (i–k) SEM images of PSK films prepared as in panels (a–c). (l) XRD spectra of PSK films prepared as in panels (a–c).

evaporate in a controlled manner before gas quenching, resulting in increased viscosity at the start of the gas quench. Also, by increasing the distance between the N_2 gun and the sample, the impact of the N_2 flow on the sample is lowered. Figure 3a–c and d–f shows the images of samples fabricated with a N_2 gun distance of 2 and 5 cm, both with natural drying times of 50, 70, and 90 s. All samples quenched at a distance of 2 cm showed visible fluid flow patterns. These flows likely stem from the sharp gas pressure gradient caused by the N_2 gun's proximity to the sample, in combination with potentially surface tension-induced flows. When the natural drying time is increased, the red circle becomes smaller and appears darker,

probably due to a lower solute flow, which is likely caused by an increased viscosity at the start of the gas quench. This interpretation is supported by profilometry measurements of the PSK film thickness beneath the N_2 gun position during gas quenching (i.e., within the circular region in Figure 3a–c), as shown in Figure S1a–c. Note that the thickness variations in Figure S1a–c are due to wavy fluid flow patterns (as seen in Figure 3a–c). The smaller and darker red circles in Figure 3b,c are associated with thicker PSK films compared to Figure 3a. Nevertheless, the film, at 90 s, still remains highly nonuniform. When increasing the N_2 gun distance, the impact of the N_2 flow clearly decreases, as visible in Figure 3d–f. This trend is

further supported by the profilometry data in **Figure S1**, which shows increased film thickness with increasing N₂ gun distance—consistent with less material being displaced by the gas flow. Regarding the samples with a 5 cm distance, a transition from a solute flow-patterned PSK film at 50 s to a smoother PSK film at higher natural drying times is observed. At 70 s, the circular shape of the N₂ gun is still slightly observed; however, no major fluid flow patterns can be seen. At 90 s, the film is even more uniform, showing a grayish color only near the edges of the sample. The images were taken to highlight the contrast related to the drying pattern. From a different angle, the sample quenched at 90 s and 5 cm appeared completely gray across the surface, corresponding to a porous PSK film (see **Figure S2a,b**). The film thickness was to be approximately 600 nm in the middle region (see **Figure S1f**) and 900 nm near the edges (see **Figure S2c**). Except for the edge effect, the sample at 5 cm and 90 s is a uniform (but porous) PSK film. These observations suggest that at a 5 cm distance and 90 s natural drying time, the gas quenching and wet film viscosity are optimally balanced, making these conditions suitable for further parameter adjustments. Beyond controlling fluid flows, ensuring a sufficiently high nucleation rate is critical for producing a compact PSK film. According to the LaMer model, a fast increase in the level of supersaturation to the critical supersaturation level is required to obtain a compact film.¹¹ In order to achieve such a fast increase in supersaturation, rapid solvent evaporation by efficient gas quenching is necessary. Reducing the wet film thickness by increasing the nozzle path speed decreases the amount of solvent that must be evaporated under the same gas quenching conditions (5 cm and 90 s). Also, lowering the NMP concentration (which is a slower evaporating solvent than DMF) would ease solvent extraction. Furthermore, considering that the nucleation step is strongly influenced by the formation of an NMP-PbI₂ adduct, a 1:1 ratio of NMP:PbI₂ should suffice, assuming a homogeneous solution.^{12,13} In this regard, excess NMP may possibly be considered unnecessary, only slowing the solvent evaporation and thereby lowering the nucleation rate. Several groups observed the relevance of NMP-to-PbI₂ ratio in achieving a pinhole-free PSK film, varying the ratio between 0 and 1.^{14,15} A similar trend is observed by Chen et al., who showed that in a DMSO/DMF cosolvent system (in which DMSO has a similar role as NMP), a compact PSK film was obtained for ratios of 0.06 to 0.50, while pinholes were observed when using less or more DMSO.¹⁶ In this study, NMP concentrations ranging from 2.5 to 10% were tested, corresponding to NMP:PbI₂ ratios of approximately 0.33–1.3 with a 0.8 M PbI₂ precursor solution. Furthermore, the influence of the wet film thickness was studied by varying the nozzle speed between 3 and 5 cm/s. **Figure 4a–c** and **e–g** shows the images of PSK films deposited at 3 and 5 cm/s at NMP concentrations of 10, 5, and 2.5%. **Figure 4i–k** shows the SEM images corresponding to the PSK films in **Figure 4a–c**. Looking at **Figure 4a**, the PSK film still appears gray, corresponding to the porous PSK (as seen in **Figure 4i**). The same is true for the film deposited with a nozzle path speed of 5 cm/s (**Figure 4e**). When lowering the NMP concentration to 5% (**Figure 4b**), the film looks uniform and black, as would be expected for a thick and compact PSK film. The SEM image in **Figure 4j** confirms the film's compactness, demonstrating that quenching was sufficiently fast at 5% NMP and 3 cm/s. When using a nozzle path speed of 5 cm/s (**Figure 4f**), the film is semitransparent and has a

brownish color, as expected for a thinner compact PSK film with a 1.6 eV band gap. The film thickness at 3 cm/s is slightly above 600 nm (similar to the 15% NMP film in **Figure 3f**), whereas at 5 cm/s, it is around 450 nm (**Figure 4d,h**). As expected, the nozzle path speed determines the wet film thickness and therefore also affects the PSK film thickness. When the NMP concentration is further decreased to 2.5% (**Figure 4c**), the films start to show irregularities, reducing the film uniformity. Looking at **Figure 4k**, needle-shaped crystals up to several micrometers in length are observed. The same was observed for the 5 cm/s film (**Figure 4g**). These micrometer-sized needles are expected to be PSK crystals, as the XRD spectra shown in **Figure 4k** for the different NMP concentrations appear similar and reveal no PbI₂ peak in the 2.5% film. A previous study from our group showed that natural drying without gas quenching led to the formation of fiber-like needles.¹⁷ A reduced NMP content in the precursor could lead to precrystallization prior to gas quenching, which may explain the emergence of such localized crystalline features. These visual and morphological findings highlight the crucial role of optimizing the NMP concentration to achieve uniform, pinhole-free PSK films. Uniform PSK films were achieved at a 5% NMP concentration for both 3 and 5 cm/s nozzle path speeds.

Device Performance. With a compact PSK film achieved across the sample area, the performance was evaluated in a completely scalable device stack. A p-i-n device stack of glass/indium tin oxide (ITO)/nickel oxide (NiO)/PSK/lithium fluoride (LiF)/fullerene (C60)/bathocuproine (BCP)/silver (Ag) was used. Two types of samples were fabricated to demonstrate the impact of the PSK film uniformity on the device performance (see **Table 1** for the

Table 1. Ultrasonic Spray Coating Parameters of the Two Types of Samples

sample type	substrate temperature (°C)	N ₂ gun distance (cm)	natural drying time (s)	NMP (%)	nozzle path speed (cm/s)
initial	40	2	10	15	3
final	28	5	90	5	3

ultrasonic spray coating parameters). The first sample was fabricated using the initial conditions (see **Table 1**). **Figure 5a** represents an image of the sample, clearly showing the nonuniform PSK deposition. The dark red circle is located at the top half of the sample due to the N₂ gun not being placed exactly above the middle of the sample. **Figure 5c** shows the sample design, including device efficiencies associated with the different cells. The light gray color represents NiO, the blue lines depict the ITO lines, and the dark gray rectangles indicate the Ag grid deposited on top of the PSK (shown in brown) and the ETL (not shown here). The rectangular overlap regions between the Ag and ITO lines represent the active areas of the cells, where the color indicates the PCE. The outer silver areas are used as the front contact. The PCE values clearly follow the nonuniformity of the PSK film. The cells close to the dark red circle (consisting of a compact PSK film) have efficiencies up to slightly above 17%. The cells at the bottom in the gray-colored PSK (consisting of a highly porous PSK film) have drastically lower efficiencies, even below 8%. The very large spread is clearly correlated to the nonuniformity of the PSK film. The second type of sample was fabricated using the adjusted parameters, yielding a uniform PSK film

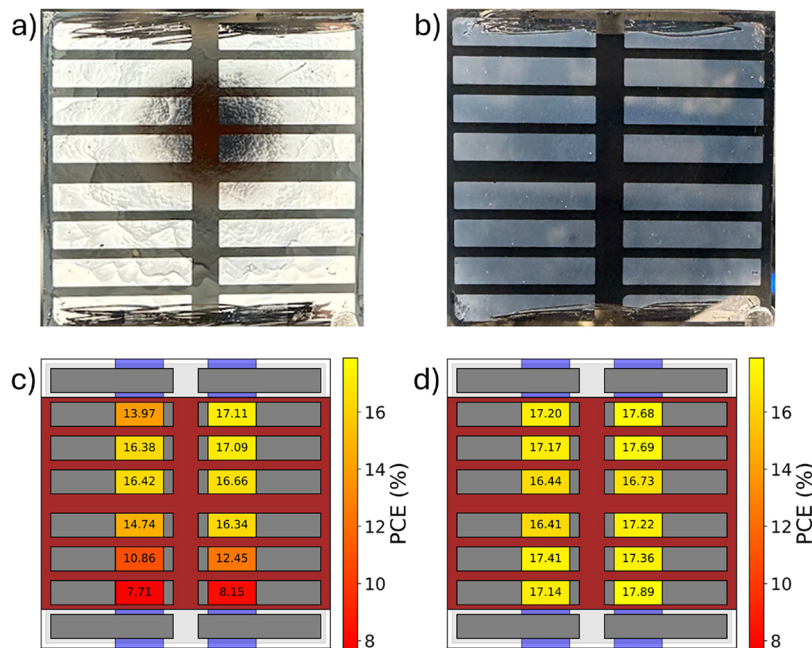


Figure 5. (a,b) Images of the $3\text{ cm} \times 3\text{ cm}$ samples corresponding to the initial and adjusted ultrasonic spray coating conditions. (c,d) Sample geometry with associated PCE values for the 12 cells of the samples in panels (a,b).

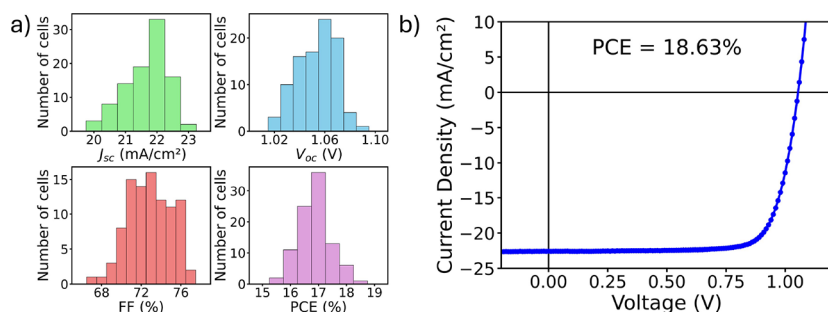


Figure 6. (a) Distribution of solar cell characteristics for a batch of 8 samples. (b) J–V curve of the champion cell.

(see Table 1). Figure 5b,d shows the images of the sample and its corresponding cell design with associated efficiencies. As can be seen, the uniform PSK film results in uniform performance across the sample area. It should be noted that the cells in the middle have a slightly lower efficiency compared to the cells closer to the edges (a difference up to 1.5%). In general, this can be understood as a minimal variation caused by the sample design. The cells in the middle are further from the front contacts (located at the edges of the ITO lines), thus exhibiting a higher series resistance and therefore a lower fill factor (see Figure S3). In addition to uniformity, the reproducibility was tested by fabricating a batch of 8 samples. Figure 6a illustrates the obtained statistics for various solar cell characteristics (measured in the reverse scan). All cells were light-soaked for at least 15 min. Figure 6b shows the reverse scan J–V curve of the champion cell, with a PCE of 18.63% (after light soaking for 30 min). The effect of light soaking is demonstrated in Figure S4 (showing 1 h of maximum power point tracking), where the normalized PCE gradually increases and stabilizes. Table 2 summarizes the solar cell characteristics of the batch (based on the 94 nondefective cells out of the 96 cells made), as well as of the champion cell. The average efficiency of 16.86% with a standard deviation of 0.57% demonstrates that the recipe is highly reproducible. To

Table 2. Solar Cell Parameters of the Batch and Champion Cell

parameter	batch	champion cell
V_{oc} (V)	1.05 ± 0.02	1.05
J_{sc} (mA/cm^2)	21.66 ± 0.68	22.58
FF (%)	72.90 ± 2.12	77.53
PCE (%)	16.86 ± 0.57	18.63

validate the device stability, two samples were remeasured after 76 days of storage in a nitrogen-filled glovebox. The solar cell parameter statistics are illustrated in Figure S5 and summarized in Table S1. On average, the cells maintained over 90% of their initial performance. To our knowledge, the champion PCE of 18.63% is among the highest efficiencies reported for ultrasonically spray-coated ~ 1.6 eV CsFAPbI_{Br} PSCs. Moreover, this work employs gas quenching—a method considered more scalable than antisolvent quenching—and a fully scalable p–i–n device architecture, featuring a sputtered NiO hole transport layer (HTL).¹⁸ The unpassivated NiO surface can easily be modified to enhance performance by simply adding a self-assembled monolayer at the NiO–PSK interface.¹⁹ This has been demonstrated in previous work by our group for

ultrasonically spray-coated PSK using exactly the same device stack.⁴

CONCLUSIONS

In this study, we demonstrated a straightforward procedure for achieving uniform and compact 1.6 eV CsFAPbI_{Br} PSK films through ultrasonic spray coating. This method relies primarily on visual inspection, supported by interpretation using concepts such as viscosity, surface-tension-induced fluid flows, and classical nucleation theory. By optimizing critical spray parameters—including the substrate temperature, N₂ gun distance, natural drying time, nozzle path speed, and NMP concentration—we effectively controlled the wet-to-dry film transition to yield uniform and compact PSK films. This was accomplished by enabling rapid drying for film compactness while controlling the drying process to reduce fluid flow in the wet film, which can disrupt the uniformity. To further improve thickness uniformity, we propose the incorporation of small amounts of surfactants or fluid-balancing agents into the precursor solution. Device performance testing confirmed that the uniform PSK films resulted in consistent performance across the sample. Furthermore, the recipe proved to be highly reproducible, yielding stable PCE values around 17%, with a champion cell reaching 18.63%. This work establishes a reliable, single-step ultrasonic spray coating process for fabricating efficient PSK films and highlights the importance of carefully controlling the wet-to-dry film transition in PSK ultrasonic spray coating. These findings contribute to ongoing efforts toward scalable and reproducible high-performance PSCs.

EXPERIMENTAL SECTION

Sample Fabrication. The substrates used are 3 × 3 cm glass slides coated with two 150 nm thick stripes of indium tin oxide (ITO) (from Colorado Concept). Prior to any deposition, the ITO-coated glass slide is cleaned by immersion in sequential ultrasonic baths in the presence of soap solution, water, acetone, and isopropyl alcohol (IPA) for 10, 5, 5, and 5 min, respectively. The substrates were dried with a N₂ gun and transferred into a N₂ glovebox. The NiO film was deposited on ITO substrates by direct current (DC) linear sputtering from a metallic Ni target using a pure O₂ plasma at 3 mTorr and a base pressure of ~10⁻⁸ Torr, using a Nebula cluster system designed by Angstrom Engineering Inc. Subsequently, NiO was annealed in air at 300 °C for 20 min. Next, PSK was deposited using an ultrasonic spray coater (from Sono-Tek) equipped with an Impact nozzle (Sono-Tek). The PSK composition used is Cs_{0.18}FA_{0.82}Pb(I_{0.94}Br_{0.06})₃, corresponding to a 1.6 eV band gap PSK. Lead(II) iodide (PbI₂) (from TCI), formamidinium iodide (FAI) (from GreatCell Solar), and cesium bromide (CsBr) (from abcr) are diluted in a mixture of dimethylformamide and N-methyl-2-pyrrolidone (both from Sigma-Aldrich) with a concentration of 0.8 M (corresponding to the Pb molarity). All solutions are stirred overnight before use. The powders are weighed in a dry room with controlled low humidity, and the solution is prepared inside a N₂-filled glovebox. During all PSK depositions, the spray nozzle moved from right to left across the 3 cm × 3 cm samples. The spray path extended several centimeters beyond both edges of the sample, and the spray width—adjusted via the shroud pressure—exceeded the sample width by a few millimeters to ensure full coverage in a single pass. Unless stated otherwise, the following parameters were used for all PSK depositions: a precursor solution flow rate of 1 mL/min, a nozzle power of 3 W, a nitrogen (N₂) gun pressure of 7 bar (connected to a regulated N₂ line), a gas quenching time of 20 s, and a nozzle-to-substrate distance of 10 cm. The nozzle path speed, N₂ gun distance, substrate temperature, natural drying time, and NMP concentration are stated in the **Results and Discussion** section. The quenched PSK films are annealed at 100

°C for 30 min inside the glovebox. For the complete devices, after the ultrasonic spray coating of PSK, 0.8 nm LiF (0.1 Å s⁻¹), 15 nm C60 (0.5 Å s⁻¹), and 5 nm BCP (0.5 Å s⁻¹) were sequentially evaporated in a thermal evaporation chamber of the Nebula cluster system at a base pressure of ~10⁻⁷ Torr. Finally, 100 nm Ag electrodes were thermally evaporated at a rate of 2 Å s⁻¹ after mechanical scribing to partially expose the edges of the ITO stripes in order to obtain front contacts. A metal mask was used to define an active area of 0.125 cm² for 12 cells on the substrate (defined by the overlap between the Ag lines and the ITO underneath) and 4 front contacts. The final layer architecture of the cell is ITO/NiO/PSK/LiF/C60/BCP/Ag.

Characterization. The current–voltage (I–V) measurements and light soaking were performed by using an Abet Sun 3000 solar simulator with a Keithley 2602A source measure unit. The measurements were done in a N₂-filled glovebox under AM 1.5G illumination at 100 mW cm⁻². A silicon cell certified by the Fraunhofer ISE was used to calibrate the illumination intensity. SEM images were obtained using a TESCAN VEGA3 or NOVA200 SEM tool. Thickness measurements were performed by using a KLA Tencor D-500 profilometer. The XRD measurements were performed using a Bruker D8 diffractometer equipped with Cu–K α X-rays ($\lambda = 1.5418 \text{ \AA}$).

ASSOCIATED CONTENT

Supporting Information

The Supporting Information is available free of charge at <https://pubs.acs.org/doi/10.1021/acsaem.Sc00718>.

Height measurements (profilometry) of spray-coated films; additional photograph and SEM image; J–V curve analysis for uniformity; maximum power point tracking data; and long-term storage stability data ([PDF](#))

AUTHOR INFORMATION

Corresponding Author

Joost Caeyers — Imec, imo-imomec, 3600 Genk, Belgium;
Hasselt University, imo-imomec, 3500 Hasselt, Belgium;
EnergyVille, imo-imomec, 3600 Genk, Belgium; [orcid.org/0009-0006-1195-5875](#); Email: joost.caeyers@imec.be

Authors

Tamara Merckx — Imec, imo-imomec, 3600 Genk, Belgium;
EnergyVille, imo-imomec, 3600 Genk, Belgium

Jessica de Wild — Imec, imo-imomec, 3600 Genk, Belgium;
Hasselt University, imo-imomec, 3500 Hasselt, Belgium;
EnergyVille, imo-imomec, 3600 Genk, Belgium; [orcid.org/0000-0003-2291-4674](#)

Wim Deferme — Imec, imo-imomec, 3600 Genk, Belgium;
Hasselt University, imo-imomec, 3500 Hasselt, Belgium;
EnergyVille, imo-imomec, 3600 Genk, Belgium; [orcid.org/0000-0002-8982-959X](#)

Bart Vermang — Imec, imo-imomec, 3600 Genk, Belgium;
Hasselt University, imo-imomec, 3500 Hasselt, Belgium;
EnergyVille, imo-imomec, 3600 Genk, Belgium

Complete contact information is available at:
<https://pubs.acs.org/10.1021/acsaem.Sc00718>

Notes

The authors declare no competing financial interest.

ACKNOWLEDGMENTS

This work was funded by Research Foundation—Flanders (FWO) through the Project Number G0A1623N (ENGAGED). The authors would like to thank Daniely Santos

(Hasselt University and IMEC) for her help with the XRD measurements.

■ REFERENCES

- (1) Chou, L.-H.; Chan, J. M.; Liu, C.-L. Progress in spray coated perovskite films for solar cell applications. *Solar RRL* **2022**, *6*, No. 2101035.
- (2) Rolston, N.; Scheideler, W. J.; Flick, A. C.; Chen, J. P.; Elmaraghi, H.; Sleagh, A.; Zhao, O.; Woodhouse, M.; Dauskardt, R. H. Rapid open-air fabrication of perovskite solar modules. *Joule* **2020**, *4*, 2675–2692.
- (3) Xu, T.; Li, Y.; Cai, H.; Zhu, Y.; Liu, C.; Han, B.; Hu, Z.; Zhang, F.; Ni, J.; Li, J.; et al. Co-solvent strategy for highly efficient perovskite solar cells by spray coating. *Sol. Energy* **2024**, *272*, No. 112461.
- (4) Silvano, J.; Birant, G.; Oris, T.; D'Haen, J.; Deferme, W.; Vermang, B. Ultrasonic spray coating for the scalable fabrication of Perovskite-on-Chalcogenide monolithic tandem Devices: Approaching the 20% efficiency. *Sol. Energy* **2024**, *277*, No. 112738.
- (5) Deng, Y.; Zheng, X.; Bai, Y.; Wang, Q.; Zhao, J.; Huang, J. Surfactant-controlled ink drying enables high-speed deposition of perovskite films for efficient photovoltaic modules. *Nature Energy* **2018**, *3*, 560–566.
- (6) Yu, X.; Mo, Y.; Li, J.; Ku, Z.; Xiao, J.; Long, F.; Han, L.; Li, W.; Lei, S.; Peng, Y.; et al. Moisture control enables high-performance sprayed perovskite solar cells under ambient conditions. *Materials Today Energy* **2023**, *37*, No. 101391.
- (7) Yu, X.; Li, J.; Mo, Y.; Xiang, T.; Ku, Z.; Huang, F.; Long, F.; Peng, Y.; Cheng, Y.-B. “Coffee ring” controlment in spray prepared 19% efficiency Cs_{0.19}FA_{0.81}PbI₂.5Br_{0.5} perovskite solar cells. *Journal of Energy Chemistry* **2022**, *67*, 201–208.
- (8) Silvano, J.; Hamtaei, S.; Verding, P.; Vermang, B.; Deferme, W. Investigating the Fabrication of Perovskite Solar Cells by Ultrasonic Spray Coating: A Design of Experiments Approach. *ACS Applied Energy Materials* **2023**, *6*, 7363–7376.
- (9) Yang, C.; He, G.; He, Y.; Ma, P. Densities and viscosities of N,N-dimethylformamide+ N-methyl-2-pyrrolidinone and+ dimethyl sulfoxide in the temperature range (303.15 to 353.15) K. *Journal of Chemical & Engineering Data* **2008**, *53*, 1639–1642.
- (10) Al Tuwaim, M. S.; Al-Jimaz, A. S.; Alkhaldi, K. H. Viscosities and surface tensions of phenetole with N-methyl-2-pyrrolidone, N,N-dimethylformamide and tetrahydrofuran binary systems at three temperatures. *J. Solution Chem.* **2018**, *47*, 449–467.
- (11) Yang, F.; Jang, D.; Dong, L.; Qiu, S.; Distler, A.; Li, N.; Brabec, C. J.; Egelhaaf, H.-J. Upscaling solution-processed perovskite photovoltaics. *Adv. Energy Mater.* **2021**, *11*, No. 2101973.
- (12) Bu, T.; Li, J.; Li, H.; Tian, C.; Su, J.; Tong, G.; Ono, L. K.; Wang, C.; Lin, Z.; Chai, N.; et al. Lead halide-templated crystallization of methylamine-free perovskite for efficient photovoltaic modules. *Science* **2021**, *372*, 1327–1332.
- (13) Szostak, R.; Sanchez, S.; Marchezi, P. E.; Marques, A. S.; Silva, J. C.; Holanda, M. S.; Hagfeldt, A.; Tolentino, H. C.; Nogueira, A. F. Revealing the perovskite film formation using the gas quenching method by *in situ* GIWAXS: morphology, properties, and device performance. *Adv. Funct. Mater.* **2021**, *31*, No. 2007473.
- (14) Rajakaruna, M.; Chung, J.; Li, Y.; Saeed, M. M.; Mariam, T.; Amonette, E.; Rahimi, A.; Fu, S.; Sun, N.; Frye, B.; et al. Precursor Ink Engineering to Implement Vacuum Extraction Method for Scalable Production of Perovskite Solar Cells. *ACS Appl. Mater. Interfaces* **2024**, *16*, 57120–57129.
- (15) Zhang, Q.; Ma, G.; Green, K. A.; Gollinger, K.; Moore, J.; Demeritte, T.; Ray, P. C.; Hill, G. A., Jr.; Gu, X.; Morgan, S. E.; et al. FAPbI₃ perovskite films prepared by solvent self-volatilization for photovoltaic applications. *ACS Applied Energy Materials* **2022**, *5*, 1487–1495.
- (16) Chen, B.; Zhengshan, J. Y.; Manzoor, S.; Wang, S.; Weigand, W.; Yu, Z.; Yang, G.; Ni, Z.; Dai, X.; Holman, Z. C. Blade-coated perovskites on textured silicon for 26%-efficient monolithic perovskite/silicon tandem solar cells. *Joule* **2020**, *4*, 850–864.
- (17) Silvano, J.; Sala, J.; Merckx, T.; Kuang, Y.; Verding, P.; D'Haen, J.; Aernouts, T.; Vermang, B.; Deferme, W. A study of quenching approaches to optimize ultrasonic spray coated perovskite layers scalable for PV. *EPJ Photovoltaics* **2022**, *13*, 12.
- (18) Ding, J.; Han, Q.; Ge, Q.-Q.; Xue, D.-J.; Ma, J.-Y.; Zhao, B.-Y.; Chen, Y.-X.; Liu, J.; Mitzi, D. B.; Hu, J.-S. Fully air-bladed high-efficiency perovskite photovoltaics. *Joule* **2019**, *3*, 402–416.
- (19) Al-Ashouri, A.; Köhnen, E.; Li, B.; Magomedov, A.; Hempel, H.; Caprioglio, P.; Márquez, J. A.; Morales Vilches, A. B.; Kasparavicius, E.; Smith, J. A.; et al. Monolithic perovskite/silicon tandem solar cell with 29% efficiency by enhanced hole extraction. *Science* **2020**, *370*, 1300–1309.



CAS BIOFINDER DISCOVERY PLATFORM™

ELIMINATE DATA SILOS. FIND WHAT YOU NEED, WHEN YOU NEED IT.

A single platform for relevant, high-quality biological and toxicology research

Streamline your R&D

CAS 
A division of the American Chemical Society